

Supplementary Materials for

Diverse rupture processes in the 2015 Peru deep earthquake doublet

Lingling Ye, Thorne Lay, Hiroo Kanamori, Zhongwen Zhan, Zacharie Duputel

Published 24 June 2016, *Sci. Adv.* **2**, e1600581 (2016)

DOI: 10.1126/sciadv.1600581

This PDF file includes:

- fig. S1. Two–point-source W-phase inversion results for the 2015 Peru earthquake doublet.
- fig. S2. Long-period waveform comparisons for the 2015 Peru earthquake doublet.
- fig. S3. Rayleigh wave MRFs for the 2015 Peru earthquake doublet.
- fig. S4. Historical earthquakes around the 2015 Peru deep doublet.
- fig. S5. Gutenberg-Richter plots for intraslab seismicity beneath Peru.
- fig. S6. Constraints on rupture dimension and rupture velocity from *P*-wave back-projections.
- fig. S7. A 400-s window *P*-wave back-projection for the 2015 Peru deep doublet.
- fig. S8. Evidence for coseismic dynamic triggering by E1 and early small earthquake at the location of E2.
- fig. S9. Comparison of teleseismic waveforms of E1 and E2.
- fig. S10. Comparison of teleseismic waveforms of E1 and E2.
- fig. S11. Finite-fault slip models and shear stress changes for Peru E1.
- fig. S12. Observed and predicted waveforms for E1 on the westward dipping fault plane (strike 157°).
- fig. S13. Observed and predicted waveforms for E1 on the eastward dipping fault plane (strike 350°).
- fig. S14. Finite-fault slip models and shear stress changes for Peru E2.
- fig. S15. Observed and predicted waveforms for E2 on the westward dipping fault plane (strike 160°).
- fig. S16. Observed and predicted waveforms for E2 on the eastward dipping fault plane (strike 350°).
- fig. S17. Comparison of back-projections for data and synthetics from inverted slip models with different rupture speeds for E2.

- fig. S18. The product of $V_I^3 \Delta \sigma_E$ for the 2015 Peru deep doublet events E1 and E2.
- fig. S19. Direct comparison of seismic radiation of the 2015 Peru deep doublet events E1 and E2.
- Legends for movies S1 and S2

Other Supplementary Material for this manuscript includes the following:

(available at advances.sciencemag.org/cgi/content/full/2/6/e1600581/DC1)

- movie S1 (.mov format). Animation of back-projections of 0.1- to 1.0-Hz *P* waves for the global station distribution and NA-EU wide-aperture network (NA) for E1.
- movie S2 (.mov format). Animation of back-projections of 0.1- to 1.0-Hz *P* waves for the global station distribution and NA-EU wide-aperture network (NA) for E2.

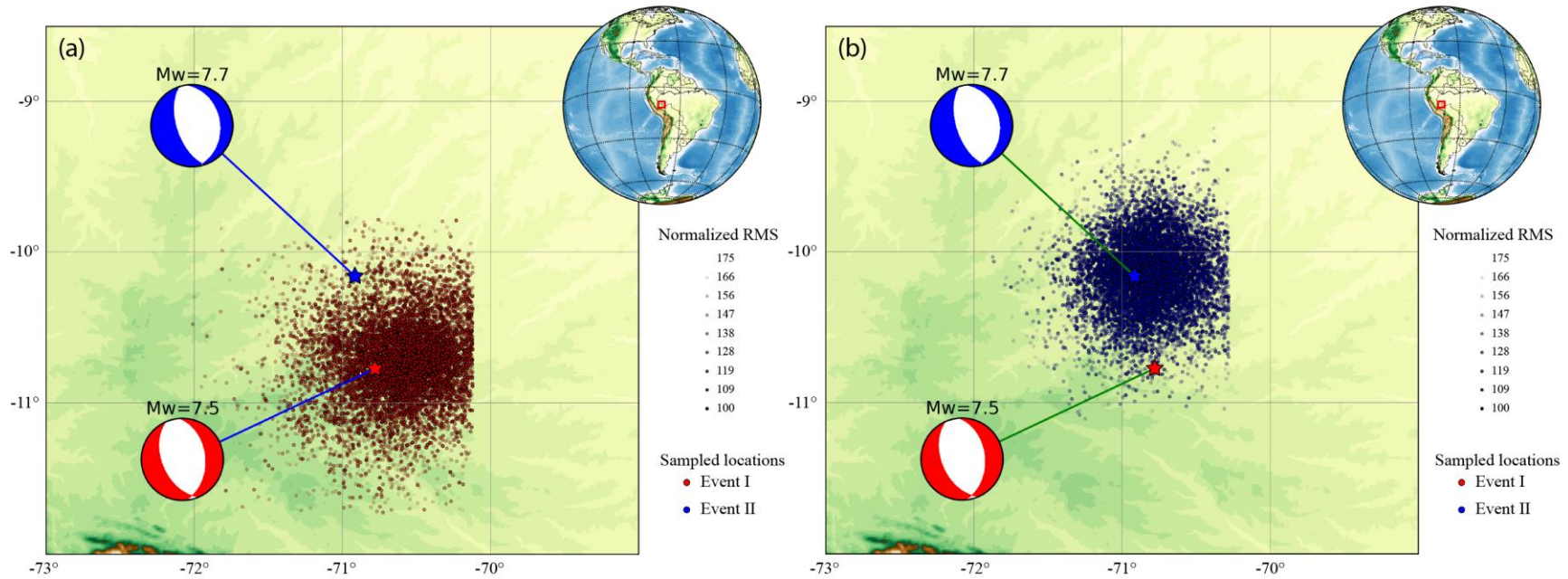


fig. S1. Two-point-source W-phase inversion results for the 2015 Peru earthquake doublet. (a) The suite of sampled hypocentral locations for E1 along with the optimal best-double couples for E1 and E2 found in the two-event W-phase inversion. (b) The suite of sampled hypocentral locations for E2. A modified version of the Neighborhood Algorithm sampler (35) was used. The transparency of the colored symbols increases with the RMS misfit normalized by the minimum value. The red and blue stars indicate the corresponding optimum centroid locations.

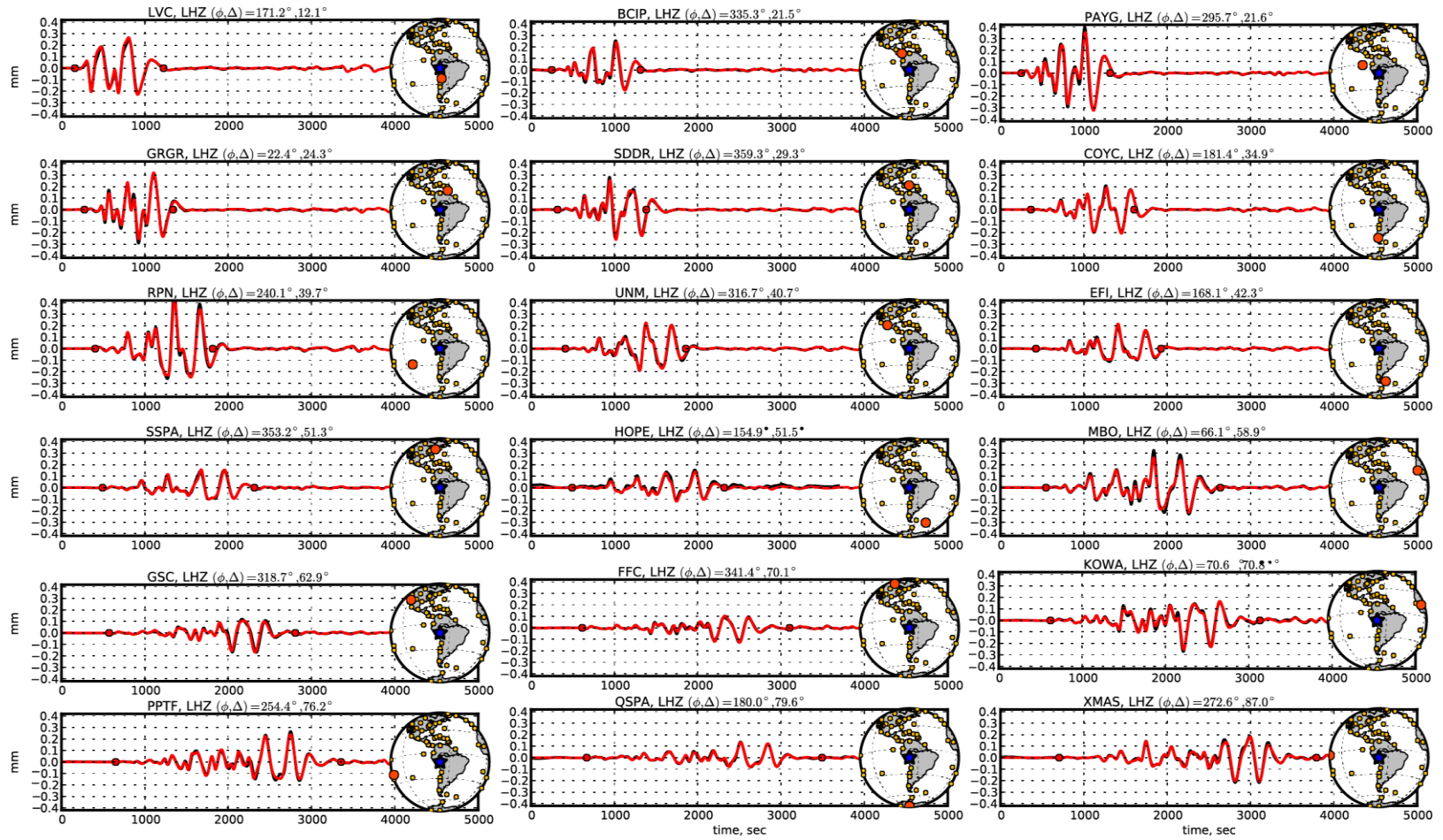


fig. S2. Long-period waveform comparisons for the 2015 Peru earthquake doublet. Examples of observed ground displacement waveforms (black lines) and corresponding synthetics (red lines) computed from the optimal two-point source W-phase inversion. The station azimuth (ϕ) and epicentral distance (Δ) are given. The time-window used in the inversion is bounded by red dots. The inset maps show the locations of all stations used with gold circles, with the specific station for the waveform shown being indicated in red. The blue stars are the locations of the doublet.

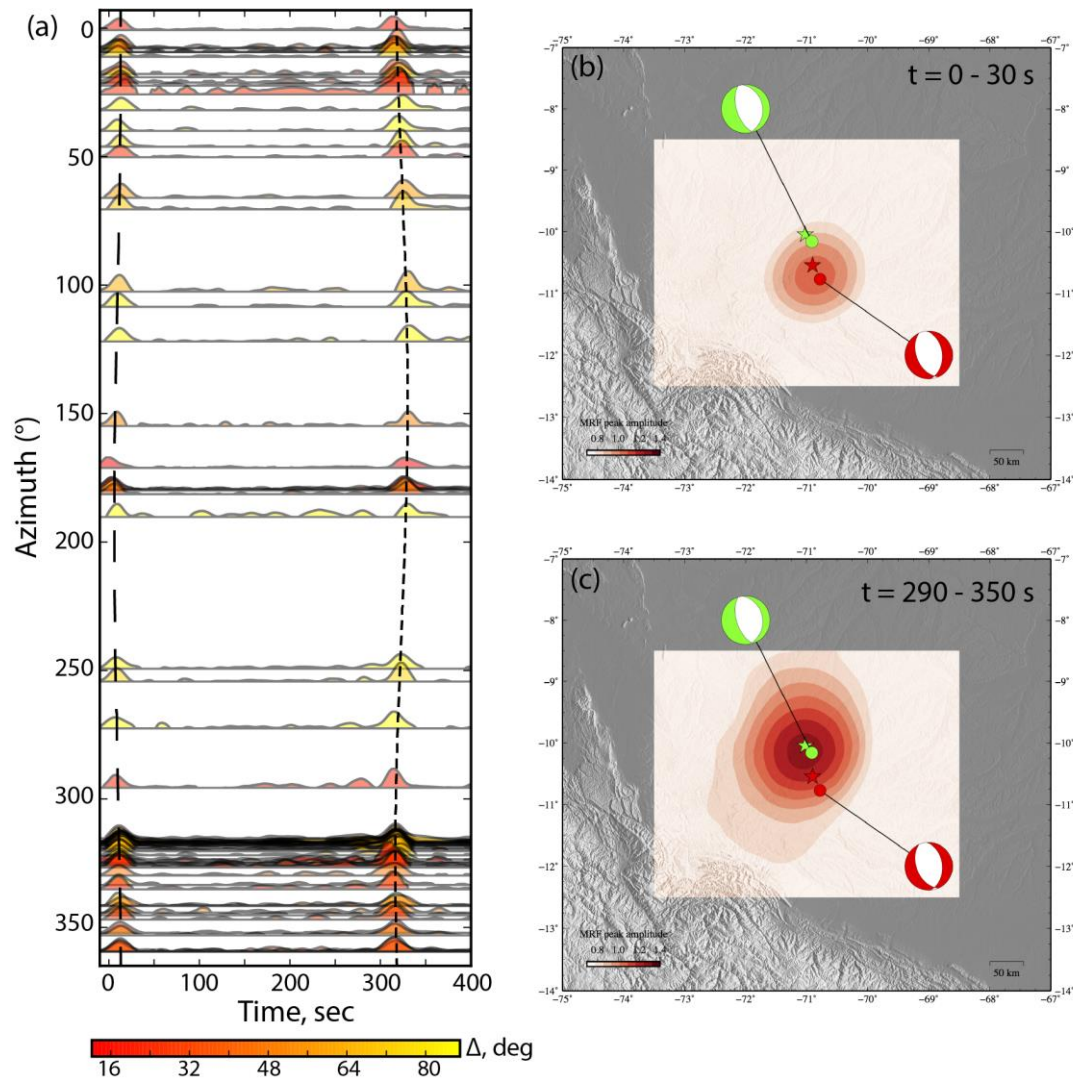


fig. S3. Rayleigh wave MRFs for the 2015 Peru earthquake doublet. (a) Rayleigh wave MRFs estimated by correcting for propagation effects plotted as a function of azimuth and colored by epicentral distance (Δ). Centroid location shifts can be inferred from the azimuthal variations in relative timing of the MRF peaks, as tracked with black dashed lines. (b) and (c) Peak stacked energy of MRFs back-projected to a gridded region around the epicenters (stars) showing the estimated centroid locations from the long-period surface wave energy. The best-double couples from the two-event W-phase inversion for E1 (red) and E2 (green) are shown with stacks for back-projection time windows spanning each event.

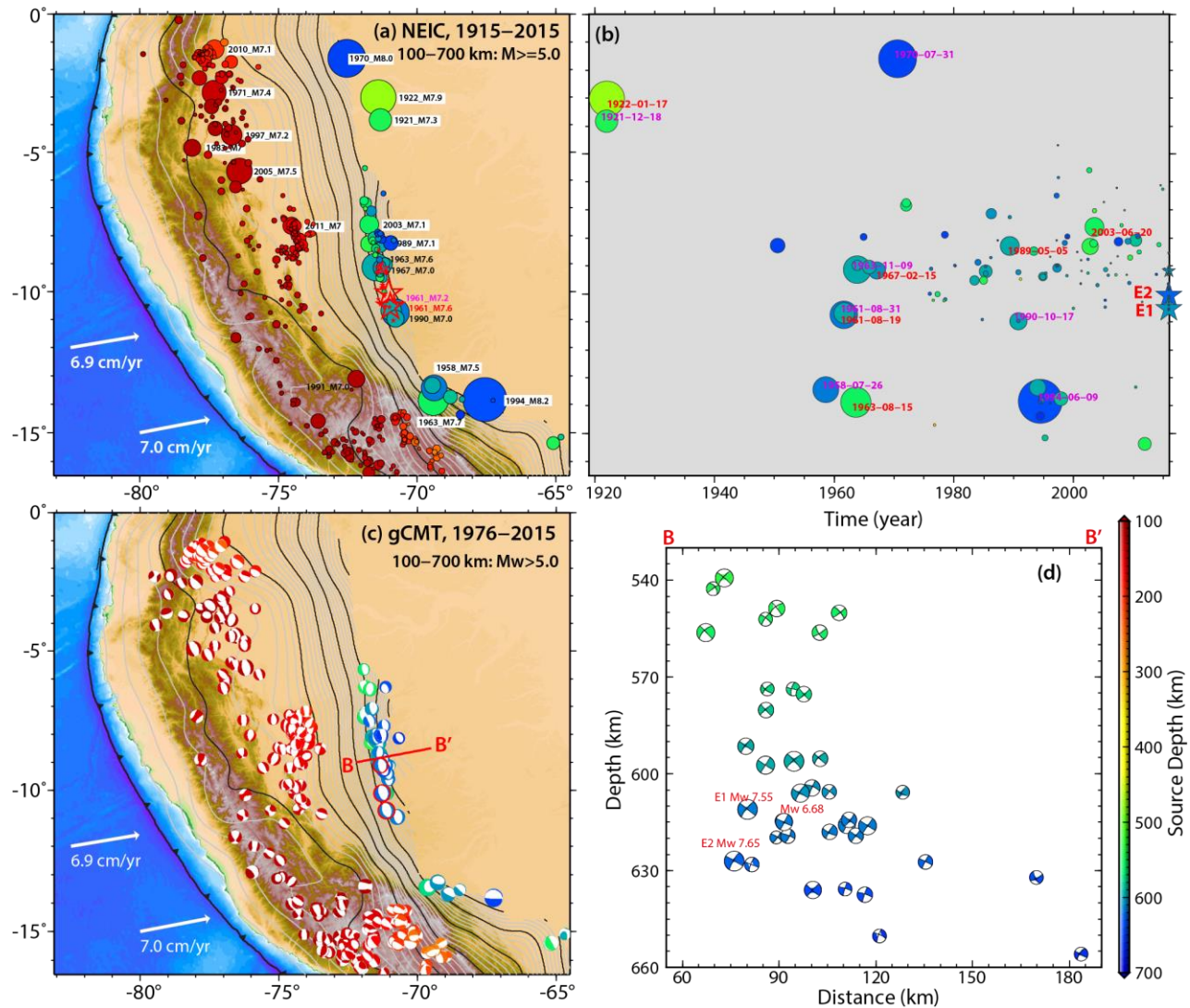


fig. S4. Historical earthquakes around the 2015 Peru deep doublet. (a) Seismicity in the slab sinking below Peru with magnitude ≥ 5.0 and source depth $\geq 100 \text{ km}$ between 1915 and 2015 from the USGS/NEIC catalog. Circles are color-coded by event depth and scaled in radius proportional to seismic magnitude. The red stars show the epicenter of the 2015 Peru deep doublet and its aftershock sequence. (b) The latitude-time distribution of deep (300 to 700 km) seismicity in (a) with symbols color-coded for event depth and scaled in radius proportion to seismic magnitude. Dates are indicated for events with magnitudes larger than 7.0. (c) All moment tensor solutions from the global Centroid-Moment Tensor catalog from 1976–2015 for depths $\geq 100 \text{ km}$, with compressional quadrants color-coded for source depth and radius scaled proportional to moment magnitude. (d) Cross-section of the deep CMT focal mechanisms along profile B-B' in (c) viewed from the horizontal perpendicular direction. The black and gray contours in (a) and (c) show the slab surface depth with 100 km and 20 km intervals, respectively. The white vectors indicate the Nazca plate motion velocities relative to a fixed South American Plate.

1970–2015 (5°S – 13°S)

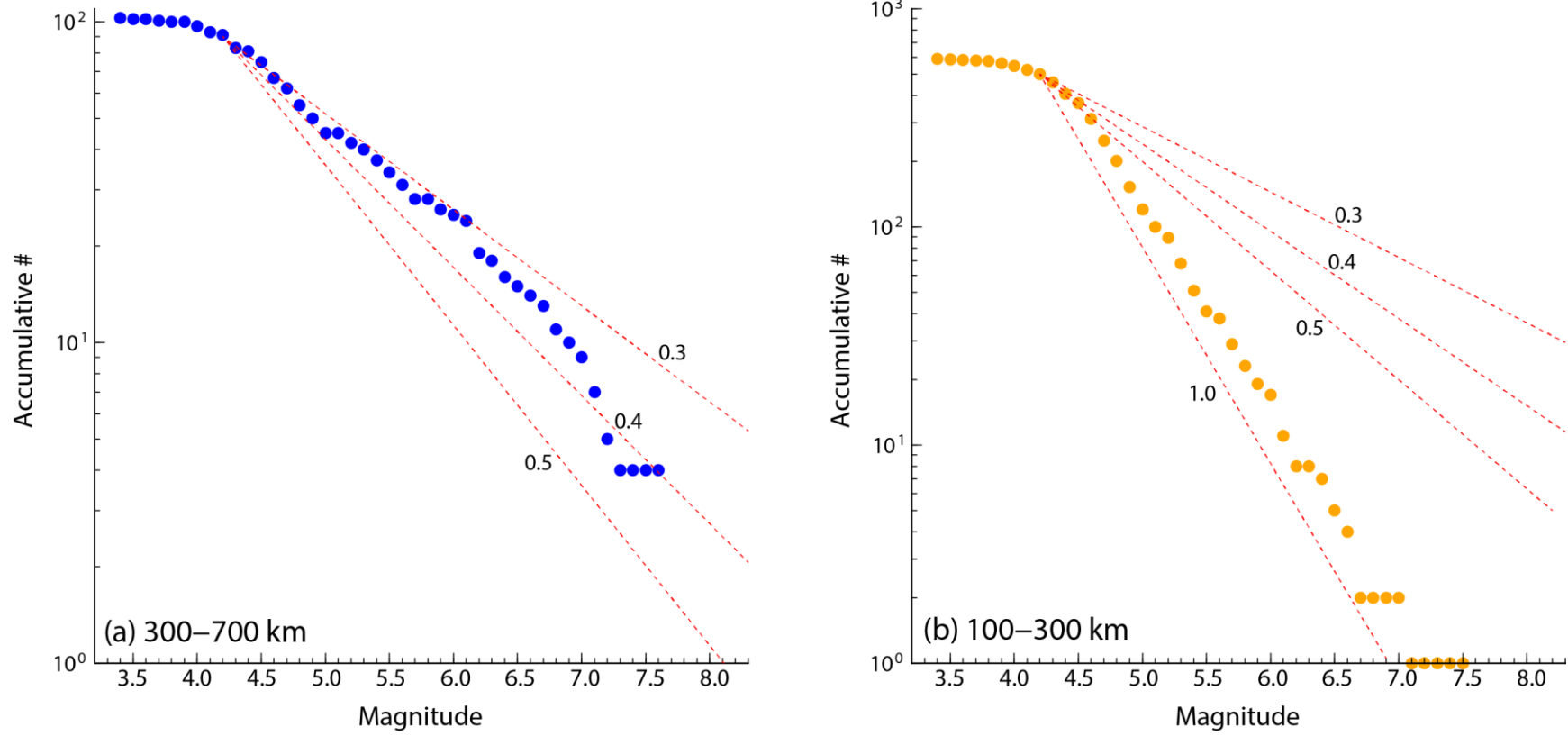


fig. S5. Gutenberg-Richter plots for intra-slab seismicity beneath Peru. The number of (a) deep-focus and (b) intermediate-depth earthquakes larger than a given magnitude versus magnitude for the latitude range 5°S to 13°S beneath Peru (fig. S4) for time period 1970 to 2015 from the USGS/NEIC catalog. The dashed lines indicated reference slopes (b-values). For deep-focus earthquakes in this region, the b-value is around 0.3-0.4 (a), whereas the b-value is close to 1 for intermediate-depth earthquakes in this region (b).

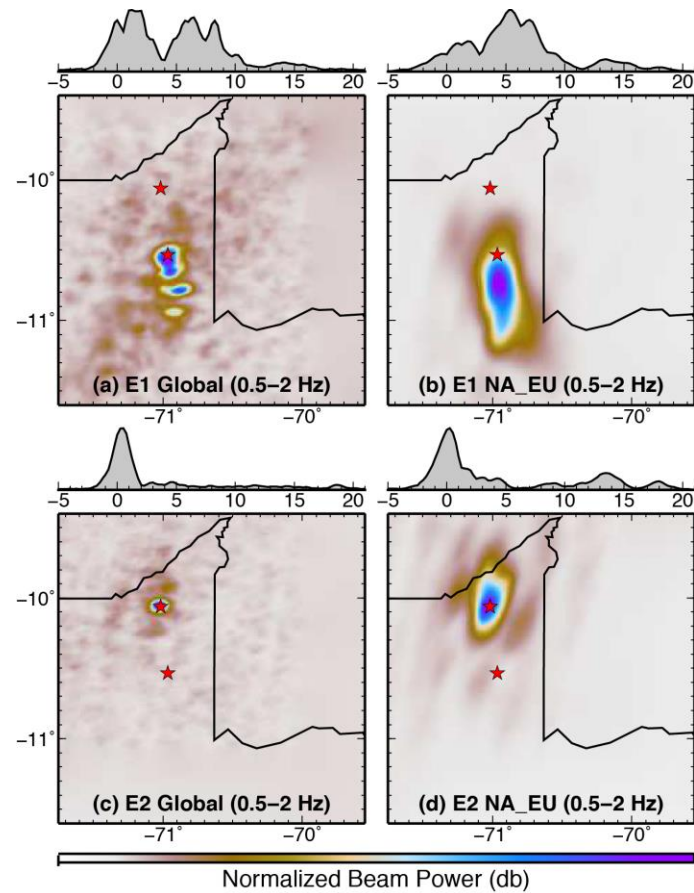


fig. S6. Constraints on rupture dimension and rupture velocity from *P*-wave back-projections. Teleseismic *P* waves in the frequency band from 0.5 to 2.0 Hz from a global distribution of stations and from North American and Europe networks (NA_EU) were used to image the coherent seismic radiation from events E1 (a), (b) and E2 (c), (d). The time-integrated back-projected signal power over a grid around the source, at its hypo central depths respectively, is shown relative to the mainshock epicenters (red stars). For E1, both global and NA_EU images indicate southward rupture extent over a distance > 50 km with a rupture propagation speed of ~4.5 km/s. Both images for E2 indicate spatially concentrated radiation without clear rupture expansion with time.

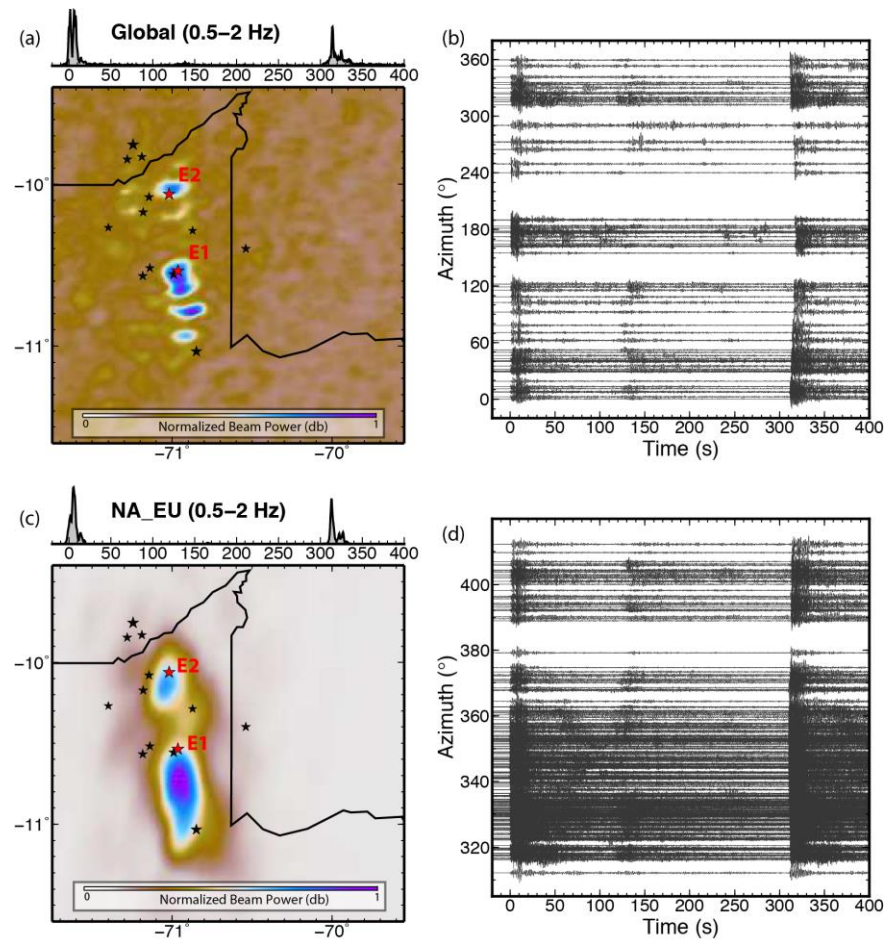


fig. S7. A 400s-window *P*-wave back-projection for the 2015 Peru deep doublet. Time-integrated back-projection of 0.5 to 2.0 Hz *P* wave beam power distributions from global (a) and NA_EU (c) networks are shown over a grid spanning both E1 and E2 at the source depth of E1. Red stars indicate the event epicenters. The time varying peak beam power is shown above each image. The black stars indicate locations of aftershocks. The corresponding filtered *P* waves from global (b) and NA_EU (d) networks aligned on the onset of event E1 plotted as a function of azimuth from the source region.

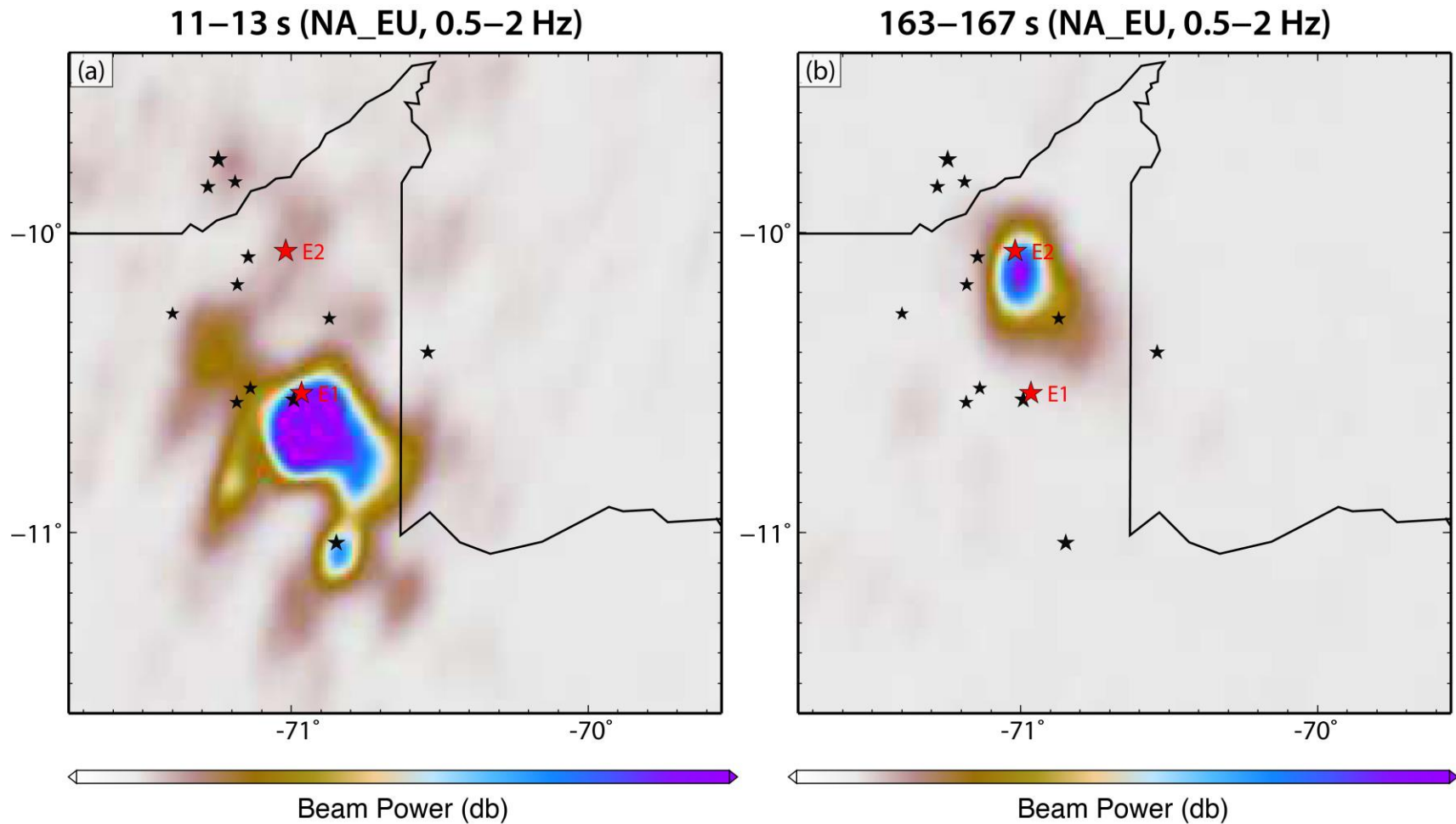


fig. S8. Evidence for coseismic dynamic triggering by E1 and early small earthquake at the location of E2. The time-integrated beam power for back-projection of 0.5 – 2 Hz teleseismic P waves from NA_EU network at (a) 11 – 13 s and (b) 163 – 167 s.

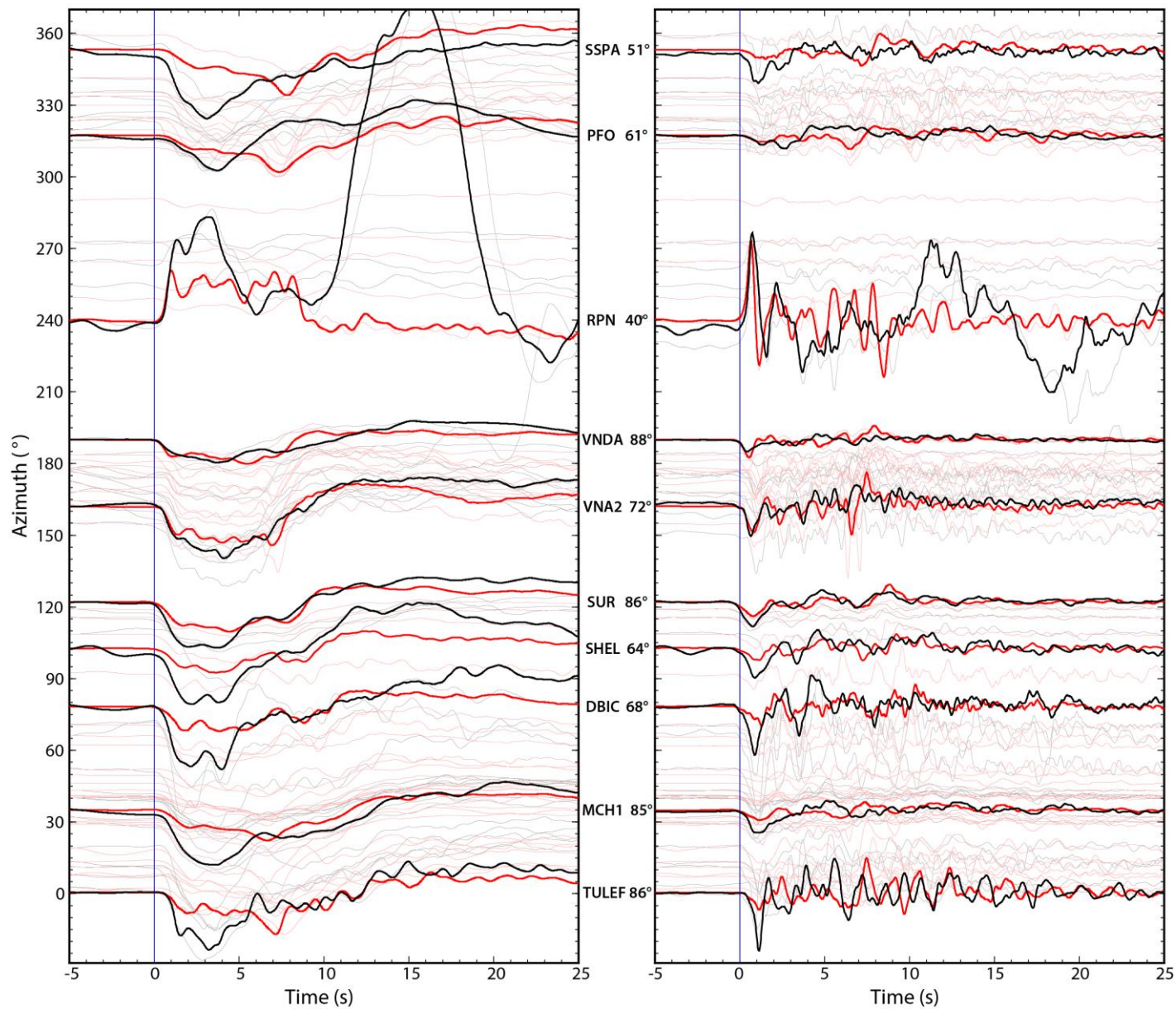


fig. S9. Comparison of teleseismic waveforms of E1 and E2. Ground displacement waveforms (left) and ground velocity waveforms (right) are plotted with true relative amplitudes for E1 (red traces) and E2 (black traces) as a function of azimuth from the source. Sample waveforms from labeled stations are shown in solid lines, and all other recordings are shown in faded lines. The large secondary arrival in the E2 waveform at RPN is the S arrival from E1.

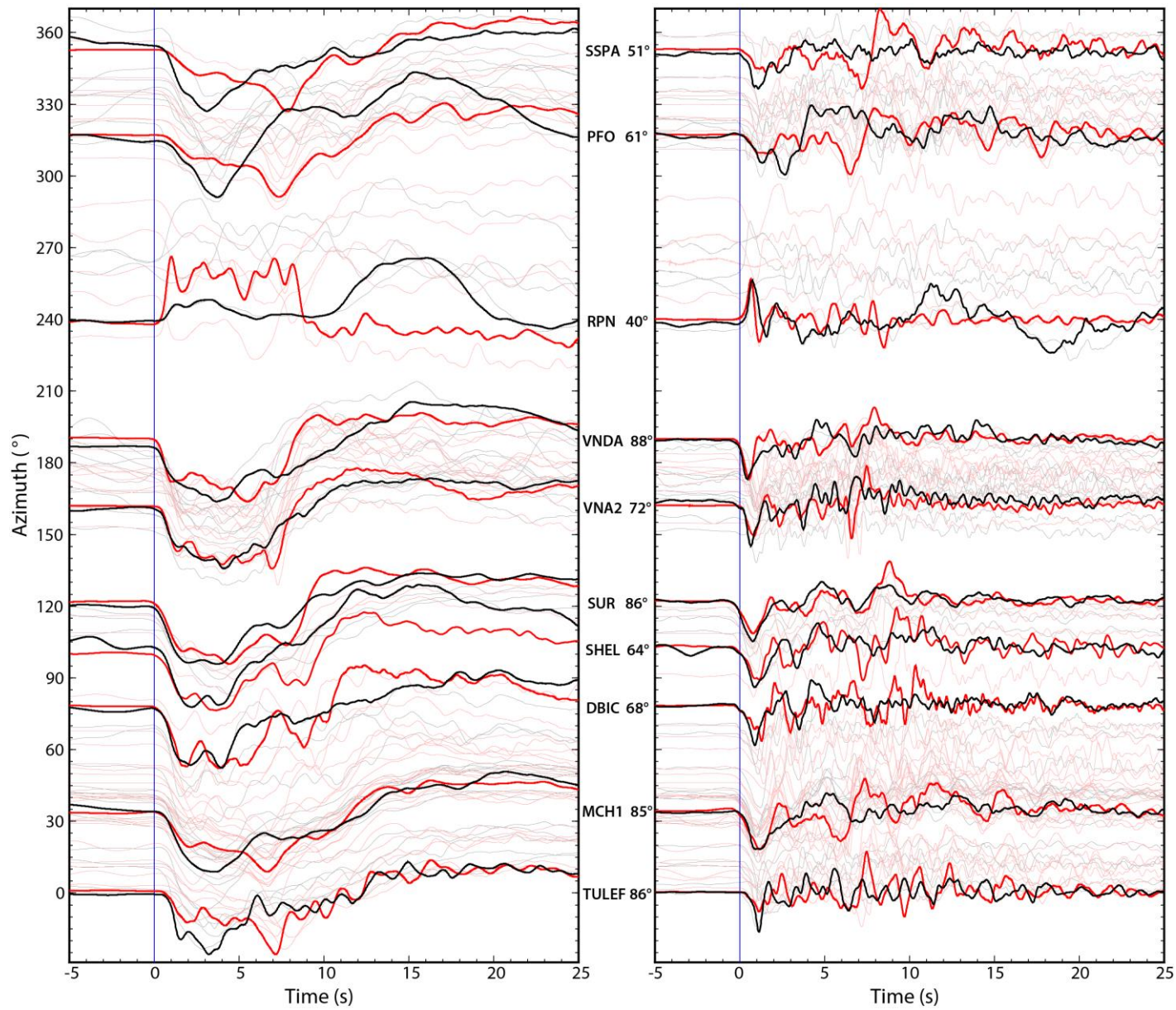


fig. S10. Comparison of teleseismic waveforms of E1 and E2. Ground displacement waveforms (left) and ground velocity waveforms (right) are plotted with self-normalized amplitudes for E1 (red traces) and E2 (black traces) as a function of azimuth from the source. Sample waveforms from labeled stations are shown in solid lines, and all other recordings are shown in faded lines.

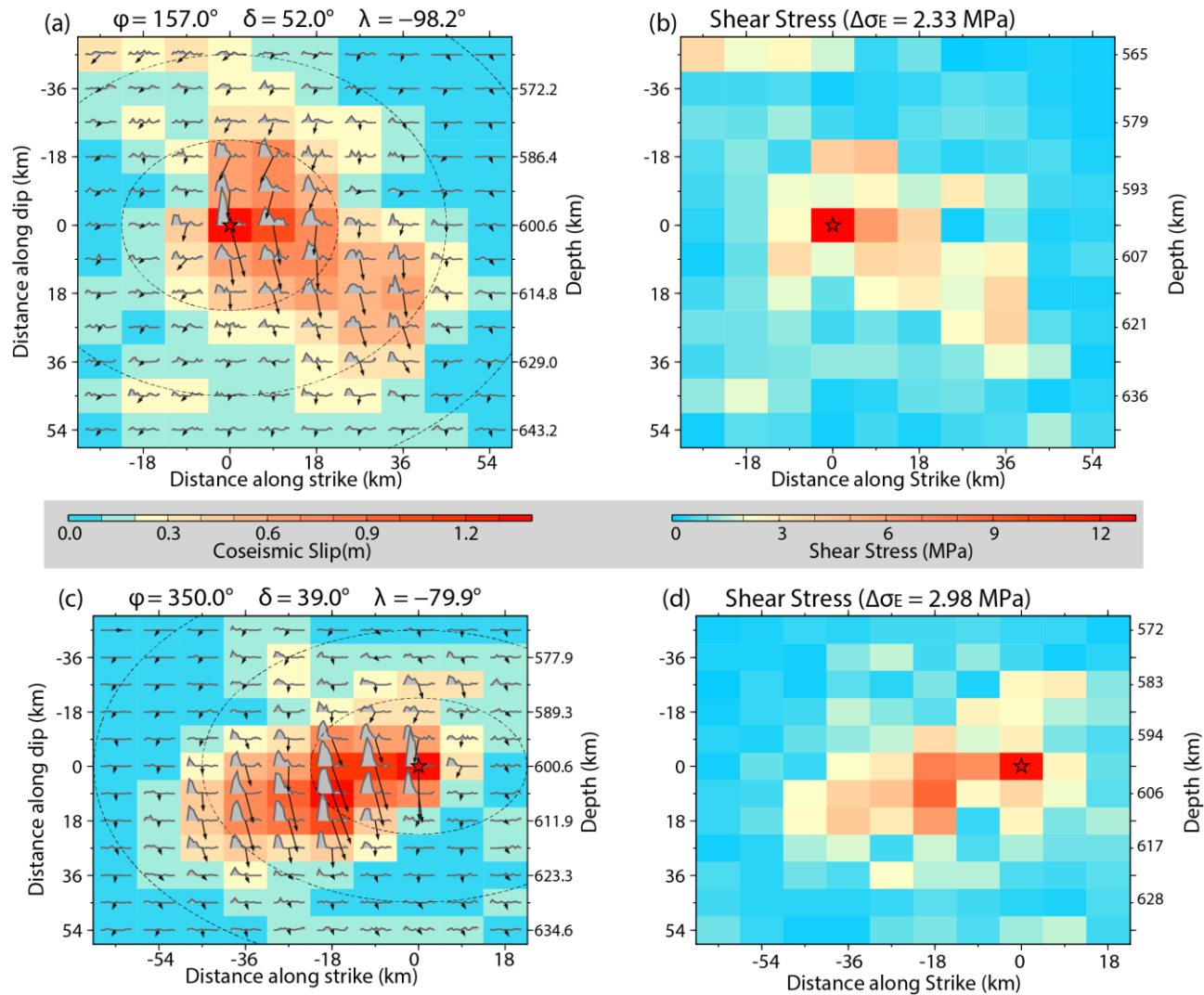


fig. S11. Finite-fault slip models and shear stress changes for Peru event E1. These models are for the westward (a, b) and eastward (c, d) dipping fault planes with indicated strike (ϕ), dip (δ) and average rake (λ), using the preferred rupture speed of 4.5 km/s and grid spacing of 9 km. Slip models (a, c) show the subfault source time functions and average slip magnitude (color scale and vector length) and direction (vector orientation in the fault-plane coordinate system). The dashed lines indicate the rupture front in 5 s intervals. (b) Shear stress distributions (b, d) are calculated at the subfault mid-points for the variable slip distributions. The average stress drops $\Delta\sigma_E$, weighted by the slip distribution (29) are 2.33 MPa and 3.0 MPa.

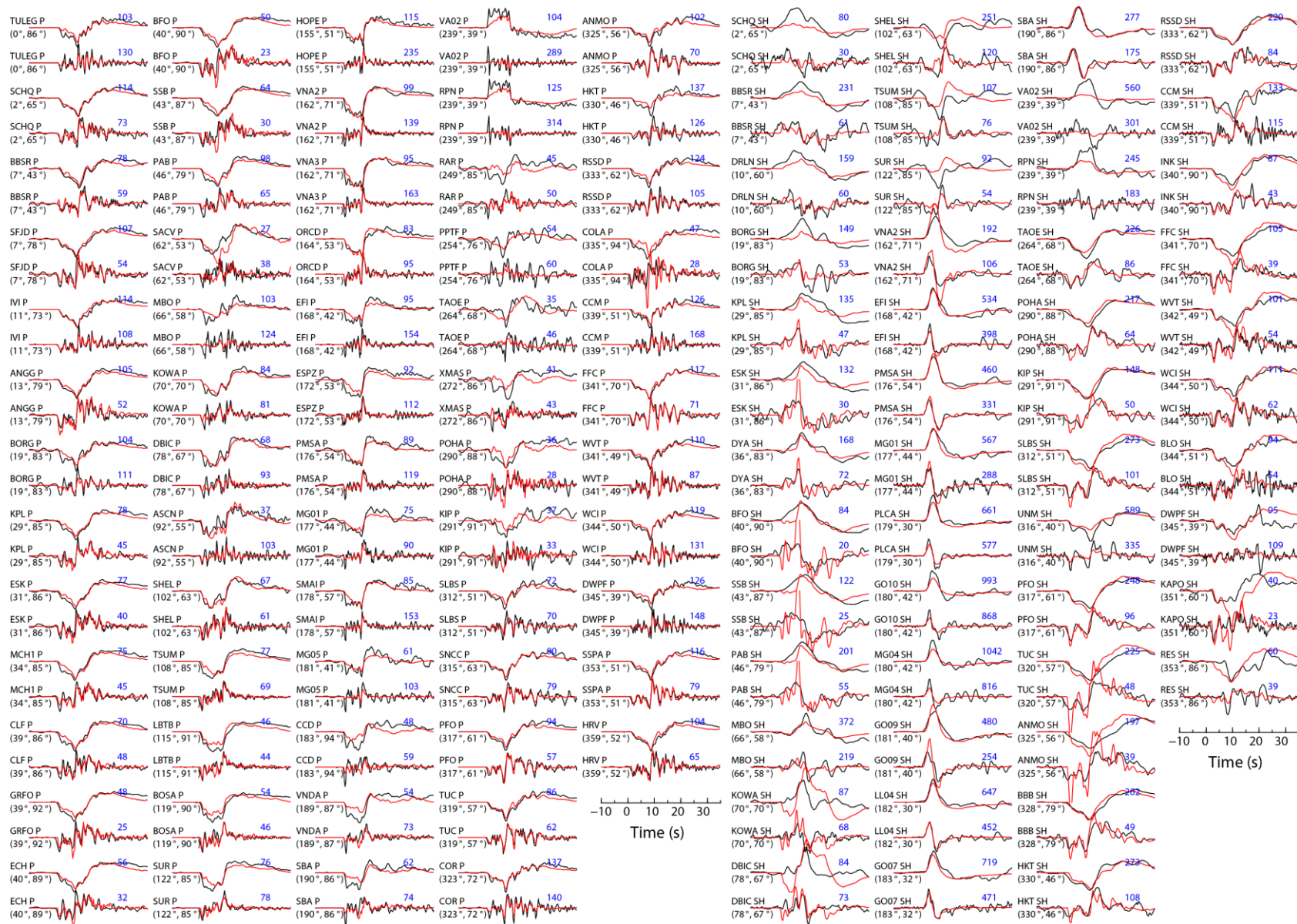


fig. S12. Observed and predicted waveforms for event E1 on the westward dipping fault plane (strike 157°). Observed (black lines) and modeled (red lines) broadband P and SH waveforms. The synthetic waveforms are for the finite-fault model in figs. 1 and S11a. For each station, both displacement (first) and velocity (second) waveforms are shown, the station azimuths and epicentral distances are indicated, along with the peak-to-peak amplitudes in microns or microns/s (blue numbers).

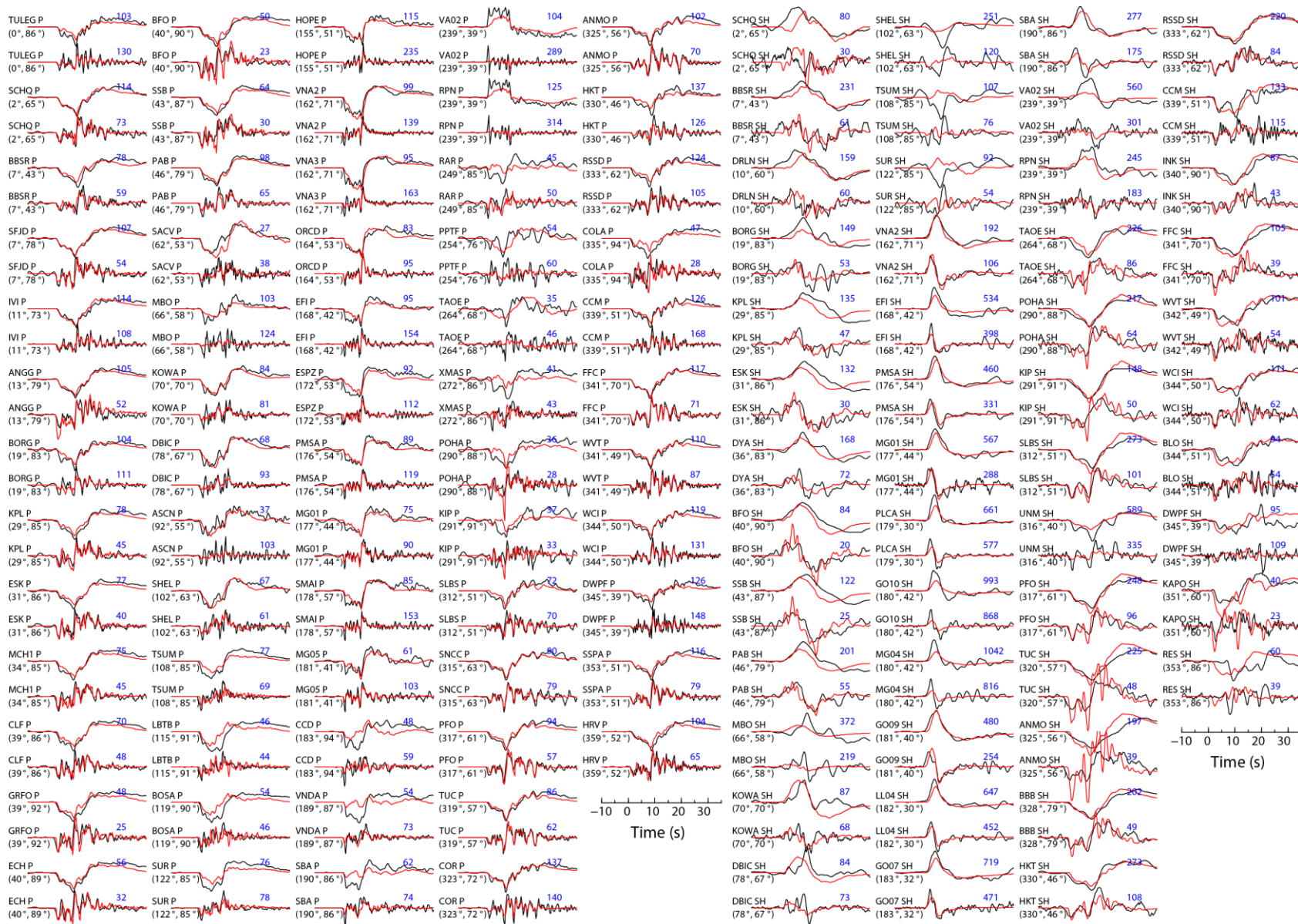


fig. S13. Observed and predicted waveforms for E1 on the eastward dipping fault plane (strike 350°). Observed (black lines) and modeled (red lines) broadband P and SH waveforms. The synthetic waveforms are for the finite-fault model in fig. S131c. For each station, both displacement (first) and velocity (second) waveforms are shown, the station azimuths and epicentral distances are indicated, along with the peak-to-peak amplitudes in microns or microns/s (blue numbers).

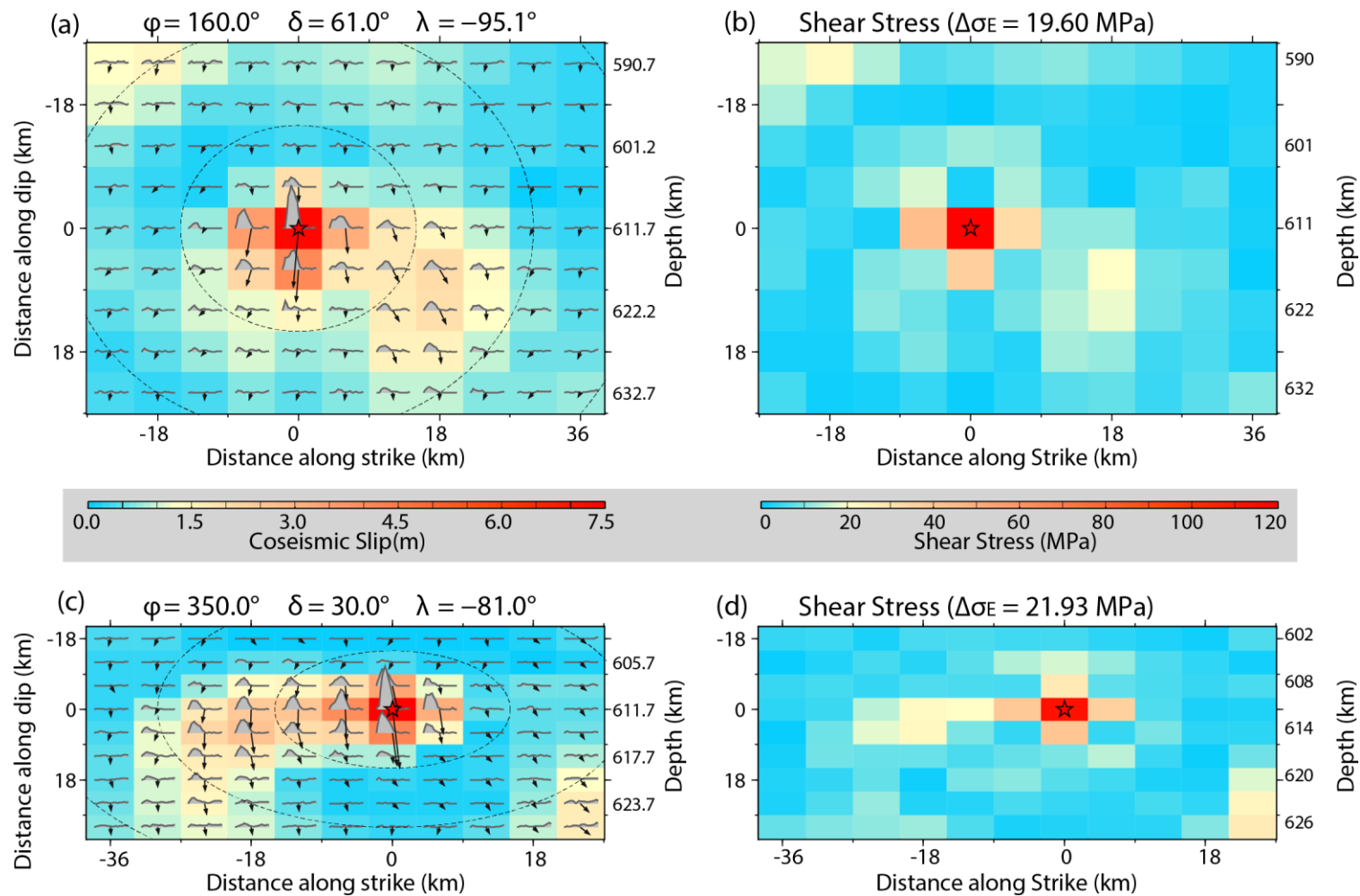


fig. S14. Finite-fault slip models and shear stress changes for Peru E2. These models are for the westward (a, b) and eastward (c, d) dipping fault planes with indicated strike (ϕ), dip (δ) and average rake (λ), using the preferred rupture speed of 3.0 km/s and grid spacing of 9 km. Slip models (a, c) show the subfault source time functions and average slip magnitude (color scale and vector length) and direction (vector orientation in the fault-plane coordinate system). The dashed lines indicate the rupture front in 5 s intervals. (b) Shear stress distributions (b, d) are calculated at the subfault mid-points for the variable slip distributions. The average stress drops $\Delta\sigma_E$, weighted by the slip distribution (29) are 19.6 MPa and 21.9 MPa.

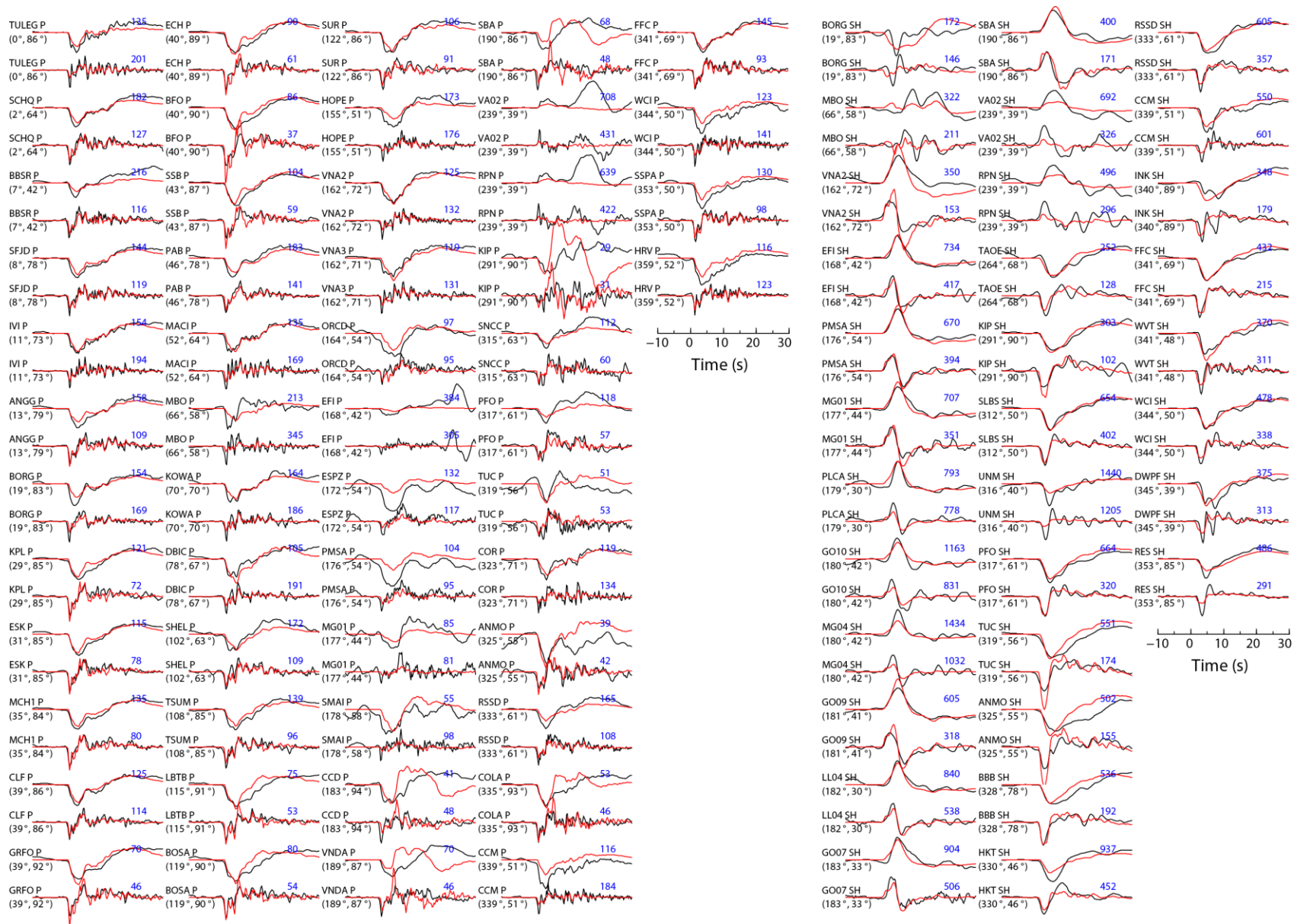


fig. S15. Observed and predicted waveforms for E2 on the westward dipping fault plane (strike 160°). Observed (black lines) and modeled (red lines) broadband P and SH waveforms. The synthetic waveforms are for the finite-fault model in figs. 1 and S14a. For each station, both displacement (first) and velocity (second) waveforms are shown, the station azimuths and epicentral distances are indicated, along with the peak-to-peak amplitudes in microns or microns/s (blue numbers).

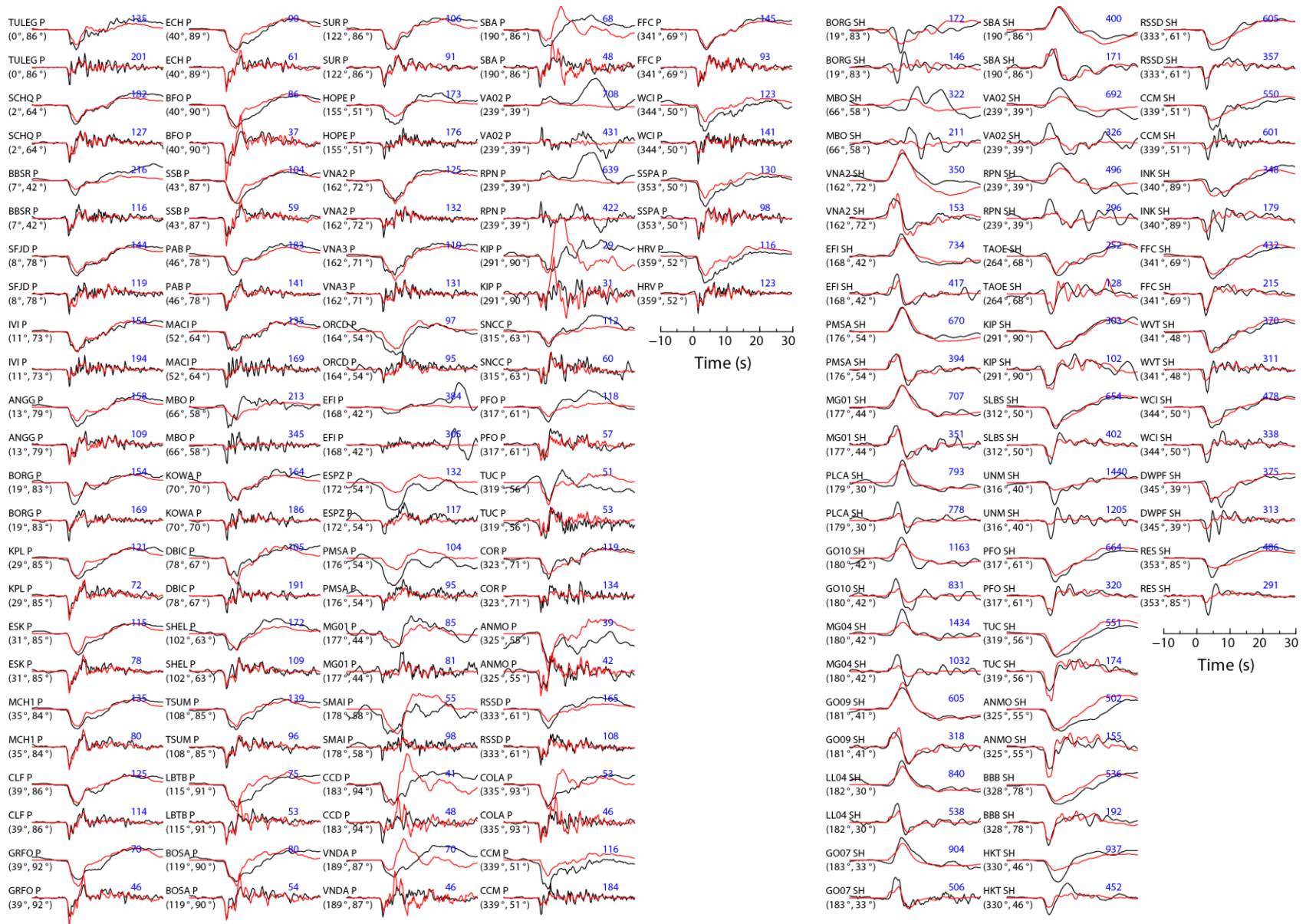


fig. S16. Observed and predicted waveforms for E2 on the eastward dipping fault plane (strike 350°). Observed (black lines) and modeled (red lines) broadband P and SH waveforms. The synthetic waveforms are for the finite-fault model in fig. S14c. For each station, both displacement (first) and velocity (second) waveforms are shown, the station azimuths and epicentral distances are indicated, along with the peak-to-peak amplitudes in microns or microns/s (blue numbers).

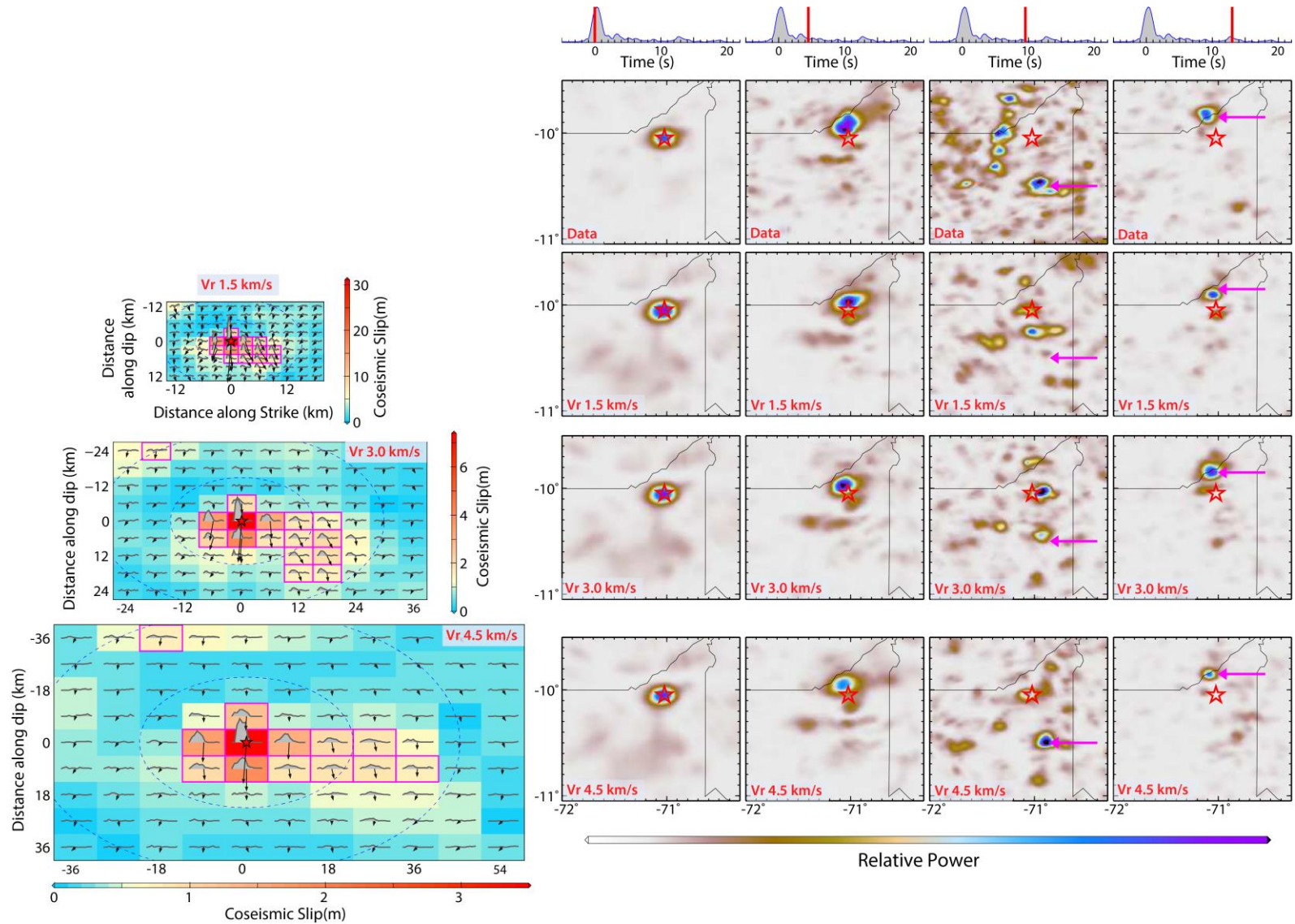


fig. S17. Comparison of back-projections for data and synthetics from inverted slip models with different rupture speeds for E2. Four snapshots of time-integrated back-projection images at 0 sec, 3-4 s, 8-10 s, and 12-13 s are shown for global 0.1-1 Hz data and synthetics for three slip models (left panels) with assumed rupture expansion speeds of 1.5 km/s, 3 km/s and 4.5 km/s. Coherent features at 8-10 s and 12-13 s to the south and north of the epicenter (red star), respectively, are highlighted by red arrows. This secondary radiation is too close to the epicenter for the model with $V_r = 1.5$ km/s compared with the data images. An additional weak feature (question mark) further to the south at 8-10 s from $V_r = 4.5$ km/s does not exist in the data image. The feature at 12-13 s has an apparent velocity from the hypocenter of 3 km/s. Thus, we prefer the slip model for $V_r = 3.0$ km/s, as an overall average rupture expansion velocity.

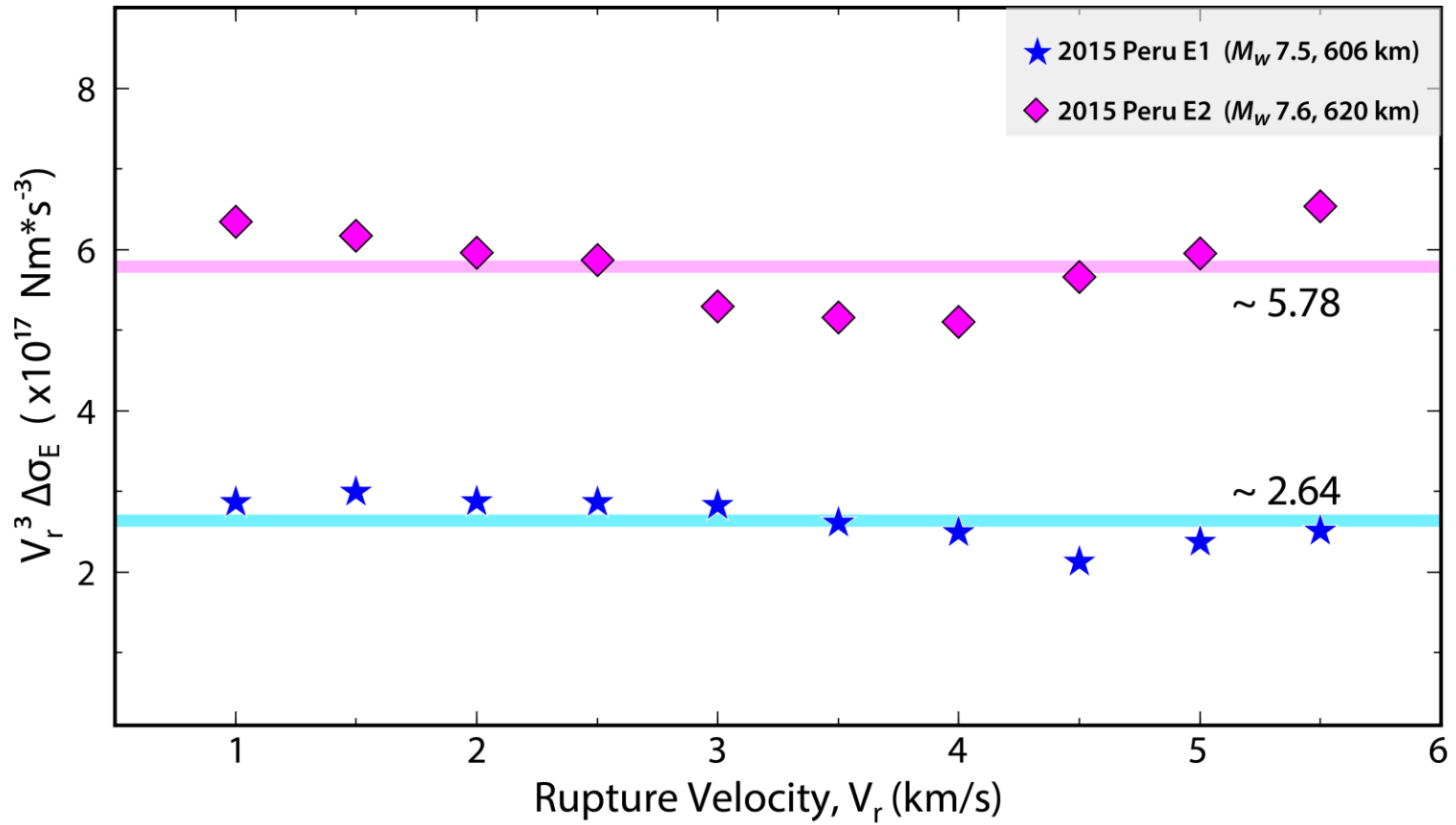


fig. S18. The product of $V_r^3 \Delta\sigma_E$ for the 2015 Peru deep doublet events E1 and E2. The static stress drop $\Delta\sigma_E$ is estimated from the finite-fault slip model with assumed rupture expansion velocity V_r . Although V_r and $\Delta\sigma_E$ cannot be constrained well individually, the product $V_r^3 \Delta\sigma_E$ can be constrained well by slip inversion, as there is little variation with assumed V_r for either E1 or E2. The cyan and magenta lines show the logarithmic averages of 2.64×10^{17} Nm/s 3 and 5.78×10^{17} Nm/s 3 for E1 and E2 respectively. A factor of ~ 2 difference between E1 and E2 is consistent with the product of $\eta_R V_r^{-3}$ shown in Fig. 5.

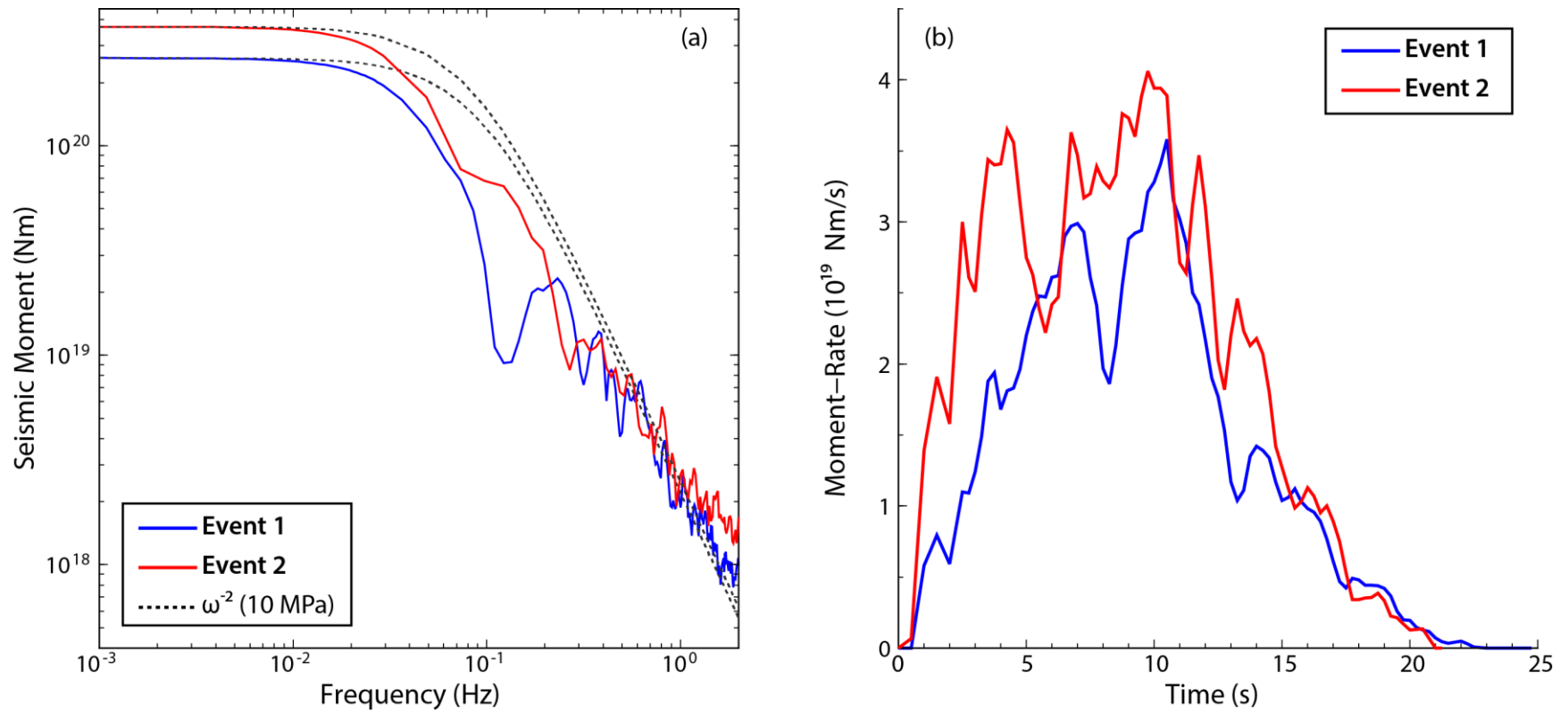


fig. S19. Direct comparison of seismic radiation of the 2015 Peru deep doublet events E1 and E2. (a) Broadband source spectra obtained from rupture slip models for frequencies below 0.05 Hz and averages of teleseismic P wave spectra for higher frequencies, and (b) moment-rate functions are shown for the 2015 Peru E1 (blue) and E2 (red). The dashed lines in (a) are reference ω -square spectra with a 10 MPa stress parameter and shear wave speed of 5.6 km/s. The trough near 0.1 Hz in the source spectrum of E1 results from the unilateral rupture boxcar-type teleseismic displacements in figs. S12 and S13. The moment-rate functions in (b) are from the finite-fault slip models shown in figs. 1, S11a, and S14a.

movie S1. Animation of back-projections of 0.1- to 1.0-Hz P waves for the global station distribution and NA-EU wide-aperture network (NA) for E1. The peak beam power at each time step is shown in the time series at the top with a marker that tracks time into the image. The map below shows the fourth-root relative beam power at each source grid position as a function of time. The star indicates the epicentral location. Power ranges from zero (white) to peak normalized value of 1 (magenta).

movie S2. Animation of back-projections of 0.1- to 1.0-Hz P waves for the global station distribution and NA-EE wide-aperture network (NA) for E2. The peak beam power at each time step is shown in the time series at the top with a marker that tracks time into the image. The map below shows the fourth-root relative beam power at each source grid position as a function of time. The star indicates the epicentral location. Power ranges from zero (white) to peak normalized value of 1 (magenta).